



HAL
open science

Load bearing performance of mechanical joints inspired by elbow of quadrupedal mammals

Aliona Sanz Idirin, Santiago Arroyave-Tobón, Jean-Marc Linares, Pedro
Arrazola

► **To cite this version:**

Aliona Sanz Idirin, Santiago Arroyave-Tobón, Jean-Marc Linares, Pedro Arrazola. Load bearing performance of mechanical joints inspired by elbow of quadrupedal mammals. *Bioinspiration and Biomimetics*, 2021, 10.1088/1748-3190/abeb57 . hal-03252973

HAL Id: hal-03252973

<https://hal.science/hal-03252973>

Submitted on 8 Jun 2021

HAL is a multi-disciplinary open access archive for the deposit and dissemination of scientific research documents, whether they are published or not. The documents may come from teaching and research institutions in France or abroad, or from public or private research centers.

L'archive ouverte pluridisciplinaire **HAL**, est destinée au dépôt et à la diffusion de documents scientifiques de niveau recherche, publiés ou non, émanant des établissements d'enseignement et de recherche français ou étrangers, des laboratoires publics ou privés.

Load bearing performance of mechanical joints inspired by elbow of quadrupedal mammals

Aliona Sanz Idirin^{1,2}, Santiago Arroyave-Tobon¹, Jean Marc Linares¹ and Pedro Arrazola²

¹ Aix Marseille Univ, CNRS, ISM, Marseille, France

² Mondragon Unibertsitatea, Arrasate-Mondragon, 20500, Euskadi, Spain

E-mail: santiago.arroyave-tobon@univ-amu.fr

Abstract

One of the biggest issues of the mechanical cylindrical joints is related to premature wear appearing. This application of bioinspiration principles in an engineering context taking advantage of smart solutions offered by nature in terms of kinematic joints could be a way of solving those problems. This work is focused on joints of one DOF in rotation (revolute or ginglymus joints in biological terms), as this is one of the most common type of mechanical joints. This type of joints can be found in the elbow of some quadrupedal mammals. The articular morphology of the elbow of these animals differs in the presence/absence of a trochlear sulcus. In this study, bio-inspired mechanical joints based on these morphologies (with/without trochlear sulcus) were designed and numerically tested. Their load bearing performance was numerically analysed. This was done through contact simulations using the finite element method under different external loading conditions (axial load, radial load and turnover moment). Results showed that the tested morphologies behave differently in transmission of external mechanical loads. It was found that bio-inspired joints without trochlea sulcus showed to be more specialized in the bearing of turnover moments. Bio-inspired joints with trochlea sulcus are more suitable for supporting combined loads (axial and radial load and turnover moments). Learning about the natural rules of mechanical design can provide new insights to improve the design of current mechanical joints.

Keywords: mechanical joints, revolute joint, elbow, articular morphology, bioinspiration, contact pressure.

1. Introduction

Kinematic joints are connections between two or more independent parts of a multibody system that allow relative motion between them. They are everywhere in natural and man-made systems: exoskeletons, endoskeletons, helicopters and robotic arms. In the medical and industrial fields, efforts of the scientific community are mainly focused on improving the lifespan of joints.

This work proposes to apply bioinspiration principles in an engineering context taking advantage of the smart solutions offered by nature regarding kinematic joints. Nature has created different types of joints with different degrees of freedom (DOF), power transmission capacity and movement ranges. These joints are characterized by specialized materials, lubrication mechanisms and articular morphologies that make them efficient and durable (Picault et al., 2018) (Egan et al., 2015).

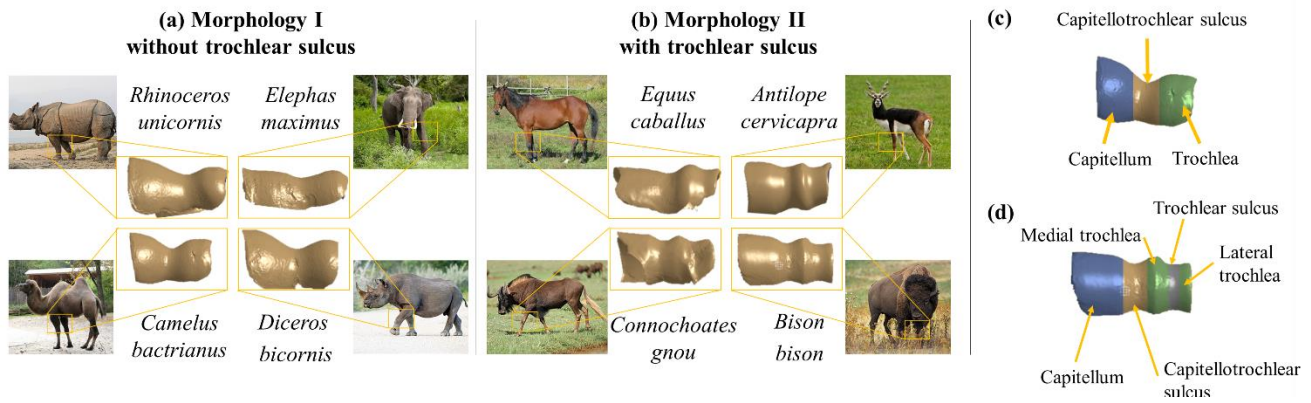


Figure 1: (a) animals whose distal humerus articulation belong to the group denominated morphology I : *Rhinoceros unicornis* (Photo by Charles J Sharp, distributed under a CC BY-SA 4.0 license); *Elephas maximus* (Photo by Yathin S Krishnappa, distributed under a CC BY-SA 3.0 license); *Camelus bactrianus* (Photo by Chrumps, distributed under a CC BY-SA 4.0 license); and *Diceros bicornis* (Photo by Yathin S Krishnappa, distributed under a CC BY-SA 3.0 license). (b) animals whose distal humerus articulation belong to the group denominated morphology II : *Equus caballus* (Photo by Tomasz Sienicki, distributed under a CC BY 3.0 license); *Antilope cervicapra* (Photo by Sagar735, distributed under a CC BY-SA 4.0 license); *Connochotes gnou* (Photo by Derek Keats, distributed under a CC BY 2.0 license); *Bison bison* (Photo by Agricultural Research Service, public domain); (c) Anatomical zones of the elbow type I. (d) Anatomical zones of the elbow type II. Images are presented at different scales. The reference numbers of the collections from National Museum of Natural History in Paris are included in Appendix A

The tribological functioning of biological joints have been widely studied (Nia et al., 2011). Their lubrication mechanisms, which are defined by interactions between the cartilage and the synovial fluid, allow them extremely low friction coefficient and therefore wear rates. However, the benefits of the geometry/topology of biological in wear performance has not been well addressed yet.

This work is focused on joints of one DOF in rotation (revolute or ginglymus joints), as this is one of the most common type of mechanical joint. This type of joint can be found in the elbow of some quadrupedal mammals. In some animals, the elbow is formed by two well defined condyles: capitellum and trochlea (hereafter called morphology I) (see Figure 1-a). In the elbow of these animals no trochlear sulcus appears. Some of the animals presenting this characteristic are, for example: *Camelus bactrianus*, *Elephas maximus*, *Rhinoceros unicornis* and *Diceros bicornis*. However, a slightly different morphology (hereafter called morphology II) can be found in the elbow of other quadrupedal mammals. This difference is the presence of a trochlear sulcus (see Figure 1-b). This is the case for example of *Equus caballus*, *Antilope cervicapra*, *Connochotes gnou* and *Bison bison*. The collection number of the analysed bones, which belong to the National Museum of Natural History in Paris, are presented in Appendix 1. To the best knowledge of the authors, no explanation has been proposed for the coexistence of these morphologies; neither a comparative analysis about their load bearing performance has been yet done. A better understanding of the coexistence of these morphologies and their functional advantages can provide new insights to improve the design of current mechanical joints.

Kinematic joints have been studied from a paleontological (phylogenetic purposes), medical (health purposes) and technological (industrial purposes) point of view, as described in the next paragraphs.

Paleontological studies have been carried out about the functionality of biological joints regarding to the evolution of the species. Concerning the elbow, several studies have been focused on the analysis of the relation between its morphology and hunting style (Andersson, 2004), locomotion (Patel, 2005) or extinction/preservation (Fujiwara, 2009) of a given species. Other research works, such as (Granatosky et al., 2019), studied the range of motion of the elbow and how it affects feeding and locomotion performance. Even if these studies help to understand evolution, they usually provide qualitative results which make their exploitation difficult in a technological context through bioinspiration.

In the medical field, several studies have been performed to evaluate load transmission in biological joints. In the case of ginglymus joints, most of these studies were conducted in the human elbow (Alcid et al., 2004; Mason et al., 2005), hand phalange (Sancho-Bru et al., 2001) and knee (Adouni et al., 2012; Amirudin et al., 2014; Haut Donahue et al., 2002; Masouros et al., 2010; Mesfar and Shirazi-Adl, 2005). These studies have motivated the design and the development of prosthetic knee (Russell et al., 2018; Sathasivam and Walker, 1994), ankle (Au et al., 2008) and elbow (Cil et al., 2008; Prasad et al., 2016). Some other works have studied load transmission in animal joints, for example on horse (Becker et al., 2019; Harrison et al., 2010; Panagiotopoulou et al., 2016; Praet et al., 2012), sheep (Lerner et al., 2015; Picault et al., 2018; Poncery et al., 2019) and seahorse (Praet et al., 2012).

Limited number of scientific articles explore the technological advantages of biological joints for bioinspiration. Picault et al. (2018) analysed contact pressure distribution in a sheep elbow under few cases of physiological loading conditions. In their study, however, the behaviour of the joint regarding transmission of axial loads and turnover moments was not analysed.

In the technological field, many studies have been performed with the aim of extending the lifetime of bearings, maximizing their load bearing performance and reducing premature wear appearing. One of the biggest issues of the cylindrical joints is related to premature wear appearing due to misalignment between inner and outer races of the bearing (Hili et al., 2005; Messaoud et al., 2011). Figure 2 presents an example of cylindrical joints present in the camshaft of the combustion engine. New bearing designs have been proposed with improved roller geometry (Dragoni, 2013; Mermoz et al., 2016; Poplawski et al., 2001; Potočnik et al., 2010; Zamponi et al., 2009; Zupan and Prebil, 2001), improved contact surface shape (Bruyas et al., 2015; Wei et al., 2016), optimal surface finishing (Fesanghary and Khonsari, 2013; Gherca et al., 2013; Lin, 2001; Qiu and Raeymaekers, 2015; Wang et al., 2003) and optimal dimensions (Boedo and Eshkabilov, 2003; Papadopoulos et al., 2011; Rezaei et al., 2012). Despite these technological advances, a limit seems to be reached, as they are still not enough to effectively prevent premature wear failure.

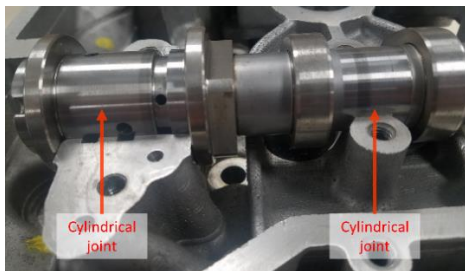


Figure 2: Example of cylindrical sliding bearings. The illustrated mechanism corresponds to the camshaft and the cylinder head of a combustion engine. The housing is made of two half parts that allow the assembly of the shaft.

Reduced number of studies exist about bearings with non-cylindrical geometry (Boedo and Eshkabilov, 2003), which might be due to associated manufacturing challenges. Nevertheless, current fabrication capabilities (additive manufacturing) are not technological barriers any more for the development of new designs.

In response to this, the aim of this study was to evaluate the load bearing performance of the two morphologies proposed by nature for the ginglymus elbow (with and without trochlear sulcus, see Figure 1). It was assumed that the load bearing performance of these morphologies is related with a combination of their topology (number of bumps) and geometry (curvature). In order to verify this, a numerical

experiment was carried out over bio-inspired joints simulating different loading conditions (radial loads, axial loads and turnover moments) using the finite element method (FEM). Load bearing was evaluated and compared by means of peak contact pressure values.

2. Methods

In this section, it is described the methodology followed to evaluate the functional advantages of the two different morphologies proposed by nature for the ginglymus elbow: morphology I (without trochlear sulcus) and morphology II (with trochlear sulcus) (see Figure 1). Bio-inspired mechanical joints based on both morphologies were designed and numerically tested. For the design of these joints, the elbows of the camel (*Camelus bactrianus*) and the bison (*Bison bison*) were selected. These two animals were chosen since their elbows have similar dimensions. The use of bones of similar dimensions allows modifying as little as possible the original dimensions of the profiles during the creation of the mechanical joints. This modification is required to obtain mechanical joints with equivalent dimensions (equal radius and length) and to make feasible comparison of their load bearing performance.

The used methodology is divided into three main steps as illustrated in Figure 3. First, bio-inspired mechanical joints were designed (Section 2.1). Second, the load bearing performance of the bio-inspired mechanical joints were numerically analysed (Section 2.2). This simulation results are presented in Section 2.3.

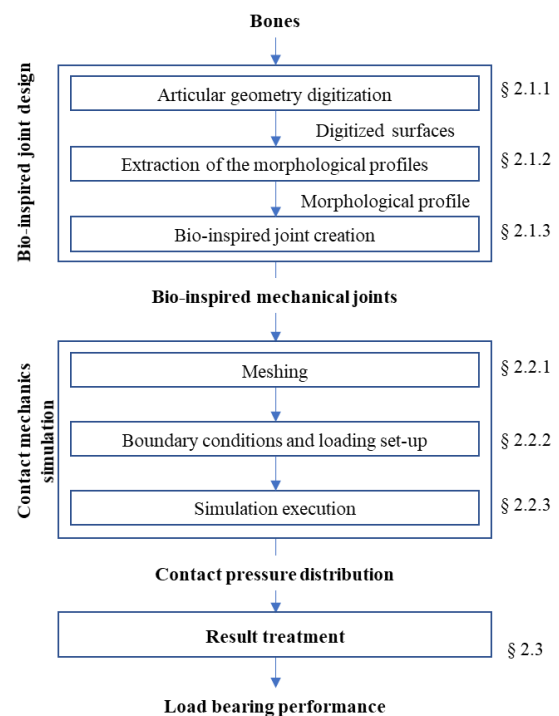


Figure 3: Followed research methodology.

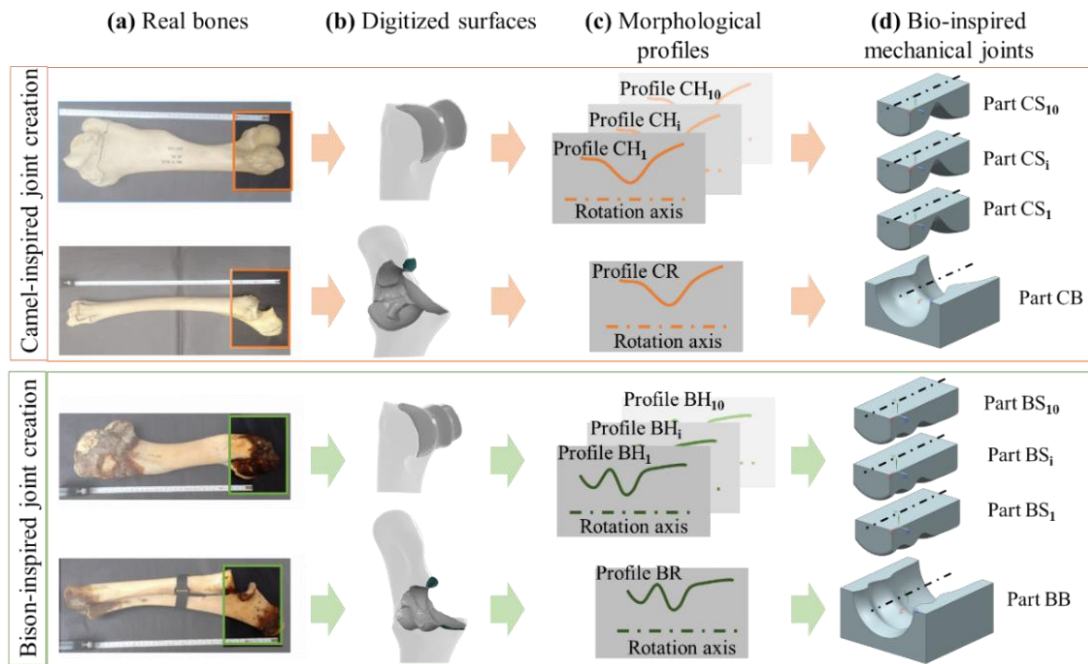


Figure 4: Followed process for the creation of the bio-inspired joints from camel and bison elbow. (a) Humerus and radius-ulna real bones; (b) humerus and radius-ulna 3D surfaces; (c) morphological profiles; (d) bio-inspired joints. Images are presented at different scale.

2.1 Bio-inspired joints

Two groups of mechanical joints were created: one group corresponding to the camel-inspired joints (representing the group of animals of morphology I : without trochlear sulcus) and the other corresponding to the bison-inspired joints (representing the group of animals of morphology II : with trochlear sulcus). Shafts were inspired in the camel and bison humerus, while bearings were inspired in the camel and bison radius-ulna.

The creation process of the bio-inspired joints is illustrated in Figure 4 and described in the next sections. The first step was the digitization of the articular geometry (Section 2.1.1). The second step was the extraction of the joint revolution profiles (Section 2.1.2). The last step was the creation of the bio-inspired joints (Section 2.1.3).

2.1.1. Articular geometry

Dry bone specimens (bones without soft tissue) of the left elbow of the *Camelus bactrianus* and *Bison bison* were used in this study (see Figure 4(a)). These specimens belong to the National Museum of Natural History of Paris collection (*Camelus bactrianus* reference: MNHN-ZM-AE-2007-1435; *Bison bison* reference: MNHN-ZM-AC-1951-242). The articular geometry of the specimens was digitized using a 3D optical scanner (Gom ATOS III, Braunschweig, Germany) with a resolution of 0.02 mm (see Figure 4-b). Four triangle meshes were obtained: camel humerus (85.3 thousand points), camel radius-ulna (74.6 thousand points), bison humerus (86.8 thousand points), and bison radius-ulna (96.8 million points).

These triangle meshes were subsequently converted into a surface and smoothed in a CAD software (CATIA V5, Dassault Systèmes, France).

2.1.2. Morphological profiles

Using CATIA V5, ten morphological profiles were obtained from each digitized humerus surface (camel and bison). One radius-ulna morphological profile was obtained from each digitized radius-ulna surface (camel and bison). The reason for doing so was to recreate ten different flexion-extension angular positions of the elbow. The flexion-extension angle of the elbow influences the articular contact as demonstrated by (Goel et al., 1982). The morphological profiles are depicted in Figure 5 in blue. They were obtained performing an intersection between the digitized surfaces and equiangular planes (5° of angular step) passing through the rotation axis. The 3D surfaces were considered as revolution surfaces and their axes were extracted by best fitting.

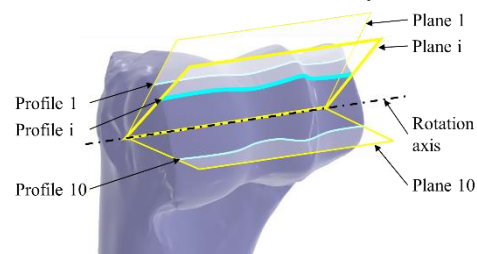


Figure 5: Extraction of morphological profiles from the distal humerus articulation. Intersection planes are represented in yellow colour, the joint rotation axis is represented in black colour and examples of morphological profiles are represented in blue.

The last step of the generation of the morphological profiles was the scaling. The objective of this scaling was to obtain equivalent mechanical joints with the same average radius and length. This is necessary to make viable the comparison of the joints in terms of load transmission. The average radius of the distal articular surface of the camel and bison humerus was of 25.3 mm and 20.1 mm respectively. Their length was of 64.3 mm and 71.7 mm respectively. A scaling was performed, and the obtained dimensions of the joints were: 68 mm of length and 22.7 mm of average radius.

The achieved morphological profiles from the camel and bison are presented in Figure 6(a) and Figure 6(b) respectively. The profile of the bearing (radio-ulna) is represented by the dotted line and with solid lines the profiles of the shafts (humerus). In Figure 6, the anatomical regions of the morphological profiles are presented for both groups. The curvature (the inverse of the radius) of the bearing profiles (derived from the radio-ulna) is presented in a light shading. These morphological profiles were used for the creation of the mechanical joints.

2.1.3. Bio-inspired mechanical joints

The bio-inspired mechanical joints were composed of two parts: shaft and bearing. For the creation of the bearings (for camel and bison), the morphological profiles coming from the radius-ulna were used. For the creation of the shafts, the morphological profiles extracted from the humerus were used. Ten shafts were created for the camel and ten for the bison. Combining the shafts with the bearing, ten mechanical joints were created.

The creation of the parts (shaft and bearing) was done by means of a revolution of the aforementioned profiles. The bio-inspired mechanical joints can be seen in Figure 7 in an exploded view with the overall dimensions of the parts. The shafts were considered to be made up of 4340 alloy steel (Young's modulus of 193000 MPa and Poisson's ratio of 0.28). The bearings were considered to be made up of polyoxymethylene (Young's modulus of 3000 MPa and Poisson's ratio of 0.35). Both materials were considered to be linear elastic and isotropic. The average mass of the camel-inspired shafts was estimated to be 325.8 g while the average mass of the bison-inspired shafts was estimated to be 306.9 g.

2.2. Contact mechanics simulation

In this section, the numerical FEM models for the contact analysis of the camel-inspired and bison-inspired mechanical joints are presented. This section is divided into three subsections. First, the meshing of the CAD models is presented in Section 2.2.1. Second, the boundary conditions and the external loads (axial load, radial load and turnover moment) are described in Section 2.2.2. Third, the execution of the simulations is explained in Section 2.2.3.

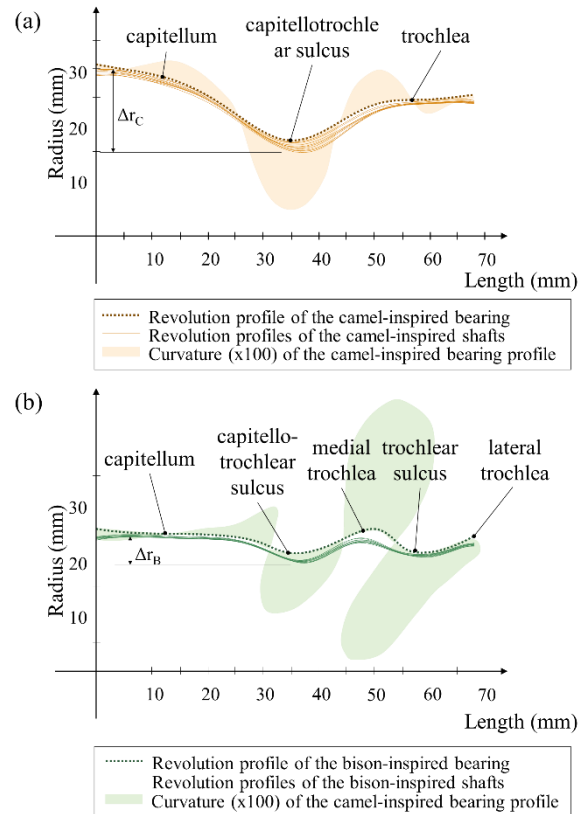


Figure 6: (a) Camel-inspired revolution profiles; (b) Bison-inspired revolution profiles. The profile of the bearing (derived from the radio-ulna) is represented by the dotted line and with a solid line the profiles of the shafts (derived from the humerus). The curvature of the bearing profiles (derived from the radio-ulna) is presented in a light shading with a scale of 100. Δr_c and Δr_b correspond to the biggest radial difference of the camel-inspired and bison-inspired profiles, respectively.

2.2.1. Meshing

The shaft and bearings were imported into NX 11.0 software (Siemens, Germany) and meshed individually using hexahedral linear elements. It was demonstrated that this type of elements behave better for contact mechanics simulations (Maas et al., 2016). A mesh convergence analysis was performed using an equivalent model made up of two cylinders. The results of the numerical simulations with the cylinders were compared with the analytical Hertzian solution. Elements with an average edge length of approximately 1 mm were found to provide an acceptable compromise between result accuracy and computational efficiency. The average number of elements, nodes and degrees of freedom per model are indicated in Table 1. The meshed models of (a) camel-inspired joint and (b) bison-inspired joint are shown in Figure 7.

Table 1: Average number of elements, nodes and DOF of the numerical models of the mechanical joints.

Model	N° of elements	N° of nodes	DOF
Camel	39600	53502	1891
Bison	41400	55393	1891

2.2.2. Boundary conditions and loading set-up

The shafts and bearings were initially assembled making coincident their rotation axes and their lateral faces parallel and aligned. All the degrees of freedom of the bottom face of the bearings were restricted. Rotation around \vec{x} and \vec{y} axes was restricted on the top face of the shafts. The inner surface of the bearings was selected as slave, and the outer surface of the shafts parts was selected as master. Unidirectional and frictionless surface-to-surface contact was defined between slave and master surfaces.

Three simulations sets were defined to evaluate the bearing performance of the created joints regarding axial loads (simulation set 1), turnover moments (simulation set 2) and combined loads (simulation set 3). For a feasible comparison, the magnitude of the applied load was the same and equal to 5.2 kN for all simulations. It was assumed that all loads act in the same plane (that normal to the \vec{z} axis) in all simulations.

In the simulation set 1, the bearing performance regarding axial loads (\vec{F}_a) was analysed. The studied range of axial load went from -2.6 kN to 2.6 kN. The direction of the force considered as positive is illustrated in Figure 7. The turnover moment was zero for these simulations. The applied radial load (\vec{F}_r) was calculated from the following relation to obtain a total constant load: $\sqrt{F_a^2 + F_r^2} = 5.2$ kN. Simulation set 1

was performed with all the joints of both groups (camel and bison-inspired joints).

In the simulation set 2, the bearing performance regarding turnover moments (\vec{M}_t) was analysed. The axial load was zero for these simulations. The studied range of turnover moment went from -138 Nm to 138 Nm. A couple of off-centred loads was applied in radial direction to obtain the desired moment value. These loads were applied at 115 mm from the center of the piece keeping a total magnitude equal to 5.2 kN. Simulation set 2 was performed with all the joints of both groups (camel and bison-inspired joints).

The simulation set 3 aimed to analyse the bearing performance regarding combined loads (axial loads and turnover moments). This simulation set was performed only with one geometry of each group (one for camel and one for bison) due to computational costs. This geometry was chosen as that whose response was the closest to the average response of all the tested geometries. The analysed range of axial load went from -2.6 kN to 2.6 kN and the analysed range of turnover moment went from -138 Nm to 138 Nm. In order to generate the desired moment, a couple of off-centred loads with a total value of 5.2 kN was applied in radial direction.

The loading conditions of each simulation set can be seen in Table 2. The conditions of the simulation set 1 (axial loads) are denominated as Sai (with $i=1:11$) and can be seen in blue colour in Table 2. The loading conditions of the simulation set 2 (turnover moments) denominated as Smj (with $j=1:12$) and can be seen in brown colour in Table 2. The loading conditions of the simulation set 3 (combined loads) are denominated as Sck (with $k=1:120$) and can be seen in black colour in Table 2.

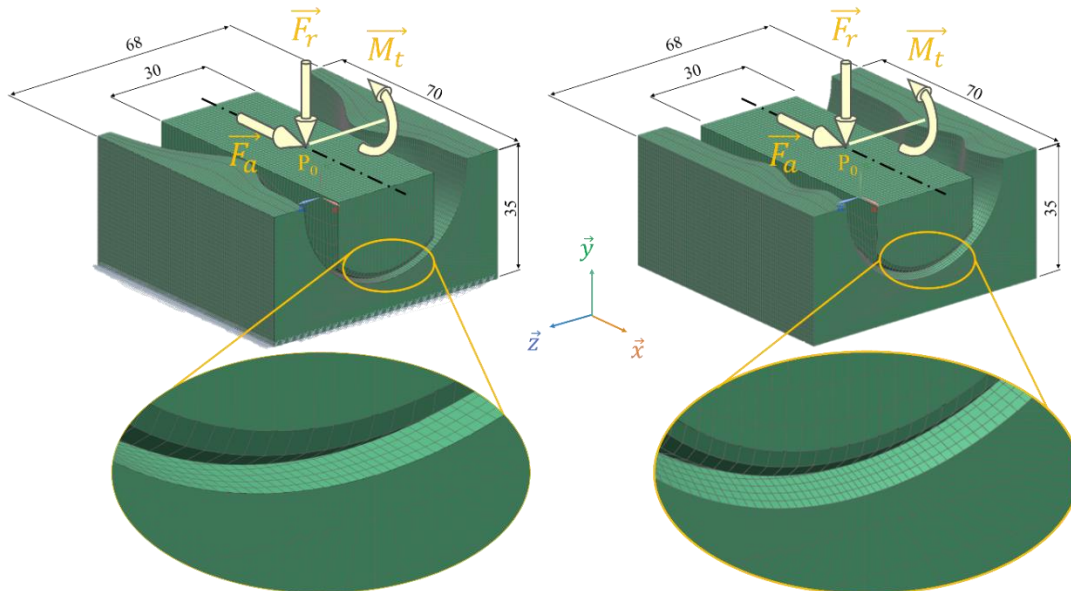


Figure 7: Example of used meshing size in (a) camel-inspired joint; (b) bison-inspired joint. A detail of the meshing is presented. P0 point indicates the midpoint of the upper face of the shaft. \vec{F}_a represents the axial force. \vec{F}_r represents the radial force. \vec{M}_t represents the turnover moment. Represented loads are assumed positive in the axis direction. Dimensions are expressed in mm.

Table 2: Loading conditions for the set of numerical simulations. F_a and F_r values are indicated on the top of the table. On the left column, M_t is indicated as a function of F_r .

F_r (kN)	4.886	5.023	5.121	5.180	5.200	5.180	5.121	5.023	4.886	4.713	4.503
F_a (kN)	-1.779	-1.346	-0.903	-0.453	0.000	0.453	0.903	1.346	1.779	2.198	2.600
M_t (Nm)											
$F_r^*(-26.5)$	Sc1	Sc13	Sc25	Sc37	Sm1	Sc49	Sc61	Sc73	Sc85	Sc97	Sc109
$F_r^*(-22.1)$	Sc2	Sc14	Sc26	Sc38	Sm2	Sc50	Sc62	Sc74	Sc86	Sc98	Sc110
$F_r^*(-17.7)$	Sc3	Sc15	Sc27	Sc39	Sm3	Sc51	Sc63	Sc75	Sc87	Sc99	Sc111
$F_r^*(-13.3)$	Sc4	Sc16	Sc28	Sc40	Sm4	Sc52	Sc64	Sc76	Sc88	Sc100	Sc112
$F_r^*(-8.8)$	Sc5	Sc17	Sc29	Sc41	Sm5	Sc53	Sc65	Sc77	Sc89	Sc101	Sc113
$F_r^*(-4.4)$	Sc6	Sc18	Sc30	Sc42	Sm6	Sc54	Sc66	Sc78	Sc90	Sc102	Sc114
$F_r^*(0)$	Sa1	Sa2	Sa3	Sa4	Sa5	Sa6	Sa7	Sa8	Sa9	Sa10	Sa11
$F_r^*(4.4)$	Sc7	Sc19	Sc31	Sc43	Sm7	Sc55	Sc67	Sc79	Sc91	Sc103	Sc115
$F_r^*(8.8)$	Sc8	Sc20	Sc32	Sc44	Sm8	Sc56	Sc68	Sc80	Sc92	Sc104	Sc116
$F_r^*(13.3)$	Sc9	Sc21	Sc33	Sc45	Sm9	Sc57	Sc69	Sc81	Sc93	Sc105	Sc117
$F_r^*(17.7)$	Sc10	Sc22	Sc34	Sc46	Sm10	Sc58	Sc70	Sc82	Sc94	Sc106	Sc118
$F_r^*(22.1)$	Sc11	Sc23	Sc35	Sc47	Sm11	Sc59	Sc71	Sc83	Sc95	Sc107	Sc119
$F_r^*(26.5)$	Sc12	Sc24	Sc36	Sc48	Sm12	Sc60	Sc72	Sc84	Sc96	Sc108	Sc120

2.2.3. Simulation execution

A total of 720 numerical simulations of contact were performed for both groups of joints (camel and bison-inspired joints). All the simulations were performed using Samcef 2015 V.17.1 (Samtech, Belgium) solver on a desktop computer (Intel (R) Xeon (R) Gold 6134, 256 Go RAM) running a 64-bit operating system. The maximum allowable penetration depth was set on 0 mm.

2.3. Result treatment

Using NX 11.0 as postprocessor, the five highest contact pressure values were averaged and considered as the peak contact pressures (P_{max}) for each simulation. This with the aim of mitigating numerical errors due to the discretisation of the geometry during the meshing process.

Confidence intervals of the mean values ($\overline{P_{max}}$) were calculated from the results of the simulations of the different geometries with the same simulation conditions. Confidence intervals were determined as twice the standard deviation (2σ). From these results, the geometry whose response was the closest to the average response of all the geometries was chosen for running the simulation set 3.

3. Results

Peak contact pressures obtained from the simulations are reported in the following sections as a function of the applied external loads (axial load, turnover moment and combined loads).

3.1. Bearing performance regarding axial loads

In Figure 8(a), $\overline{P_{max}}$ as a function of the applied axial load is presented. The applied turnover moment was zero for these simulations. In Figure 8(a), for each axial load value, central

mark points (orange triangles for camel and green circles for the bison) represent $\overline{P_{max}}$ value. The confidence interval for each set of results is represented also in Figure 8(a) (orange shading for camel and green shading for bison).

In Figure 8(a), an asymmetrical response of the $\overline{P_{max}}$ value with respect to the zero axial load value can be observed for the bison-inspired joints. The highest value of positive axial load was 65% greater regarding to the highest negative value. The camel-inspired joints had a constant and more symmetrical response, even if the capacity to support positive axial loads was slightly greater (19%) respect to the capacity to support negative axial loads. Comparing the response of both sets of joints, it can be noticed that the camel-inspired joints had a greater capacity (49% higher than bison) to support negative axial loads. Regarding to the supported positive axial loads, the bison-inspired joints had a greater capacity (18%) in comparison with the camel-inspired joints.

The camel-inspired joints had lower peak contact pressures almost in all ranges except from 2.19 kN to 2.60 kN. The $\overline{P_{max}}$ value for all simulations of the set 1 was on average 37% lower for the camel-inspired joint than for the bison-inspired joint. The minimum $\overline{P_{max}}$ value for the bison-inspired joints was 87.78 MPa, which was obtained under an axial load of -0.45 kN. The minimum $\overline{P_{max}}$ value for the camel-inspired joint was 36% lower than that of the bison, and it was obtained under axial load of 1.34 kN.

Among the ten tested joints (for bison and camel), those whose response was the closest to the average response of all the geometries were: joint N°2 (CJ₂) in the case of the camel-inspired joints group and joint N°6 (BJ₆) in the bison-inspired joints group. These two joints were used for the following analysis of the contact areas (Figure 9).

Figure 9 shows the contact distribution, from a bottom view, on the shaft of CJ₂ and BJ₆ for different values of axial loads. The bearing is represented in a wireframe. In this figure,

it can be noticed that the contact occurs mainly near the shaft ends in both BJ₆ and CJ₂. For the considered loading conditions, the deepest part of the capitellotrochlear sulcus did not enter in contact in CJ₂ neither in BJ₆. Application of negative axial loads on BJ₆ generates a high concentration of the pressure in a reduced area (edge effects). At an axial load of -1.77 kN and 2.6 kN CJ₂ presented edge effects. At axial load of -0.9 kN BJ₆ presented edge effects. At axial load of 1.77 kN, BJ₆ did not converge while CJ₂ did. The contact reaction forces could not be counteracted by the applied radial load, which generates a loss of static equilibrium and therefore of contact. For the same conditions, in most of the cases, the CJ₂ had lower P_{\max} values and larger contact areas than the BJ₆.

3.2. Bearing performance regarding turnover moments

In Figure 8(b), $\overline{P_{\max}}$ as a function of the applied turnover moments is presented. The applied axial load was zero and the radial load was 5.2 kN for these simulations. In Figure 8(b), central mark points (orange triangles for camel and green circles for the bison) represent the obtained $\overline{P_{\max}}$ for each turnover moment value, and the light shading (orange shading for camel and green shading for bison) represents the confidence interval.

In Figure 8(b), an asymmetrical response of the $\overline{P_{\max}}$ value with respect to the zero turnover moment value can be seen specially in the bison-inspired joints. On the contrary, the camel-inspired joints had more constant response. When positive turnover moments were applied, the bison-inspired joints produced lower $\overline{P_{\max}}$ (better load distribution) than when negative turnover moments were applied. The confidence intervals of the simulation results of the bison-inspired joint for negative turnover moments were larger than for positive turnover moments.

The camel-inspired joint had lower $\overline{P_{\max}}$ almost in all range except from 46 Nm to 92 Nm. The $\overline{P_{\max}}$ value for all simulations of the set 2 was on average 30 % lower for the camel-inspired joint than for the bison-inspired joint. The minimum $\overline{P_{\max}}$ value for the camel-inspired joints was obtained under turnover moment of 0 Nm. The minimum $\overline{P_{\max}}$ value for the bison-inspired joints was obtained under turnover moment of 46 Nm. Both values were almost the same around 76.85 MPa.

Among the ten tested joints for each group, CJ₂ and BJ₆ were the closest to the average response of all the geometries. Figure 10 shows the contact distribution, from a bottom view, on the shaft of CJ₂ and BJ₆ for different values of turnover moments. The bearing is represented in a wireframe. In this figure, it can be noticed that the contact occurs mainly near the shaft extremities in both cases. Also, it was seen that under the explored range of loading conditions the deepest part of the capitellotrochlear sulcus did not come in contact in CJ₂ neither in BJ₆. At turnover moments of -138 Nm and 138 Nm CJ₂ presented edge effect. At a turnover moment of 130 Nm, the

simulation with BJ₆ did not converge while CJ₂ did. The static equilibrium could not be satisfied under the applied conditions in that case. The contact reaction forces could not be counteracted by the applied radial load, which generates a loss of static equilibrium and therefore of contact. In most cases, the CJ₂ had lower P_{\max} values and larger contact areas than the BJ₆.

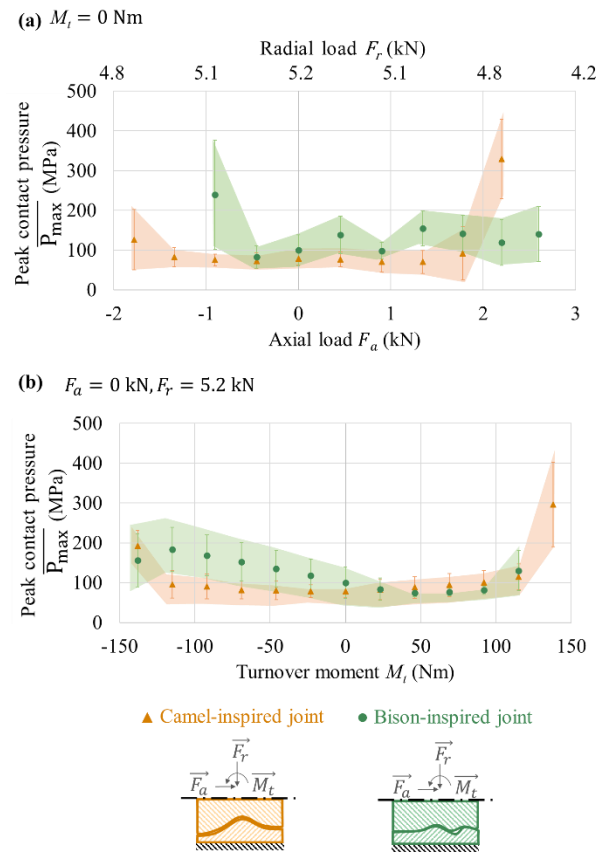


Figure 8: (a) Peak contact pressure values as a function of axial load are presented for the ten camel and bison-inspired joints. A secondary axis represents the applied radial load. (b) Peak contact pressure values as a function of turnover moment are presented for the ten camel and bison-inspired joints. The central markers (orange triangles for the camel and green circles for the bison) represent $\overline{P_{\max}}$ value for each turnover moment value and the light shading (orange shading for the camel and green shading for the bison) represent the confidence intervals.

3.3. Bearing performance regarding combined loads

In Figure 11, it can be seen P_{\max} as a function of the applied axial load and turnover moment for CJ₂ and BJ₆. In the left-hand side of this figure, it can be seen that CJ₂ behaves well (lower peak contact pressure values) under positive turnover moments if the axial load is also positive, and under negative turnover moments if the axial load is also negative. It can also be seen that BJ₆ behaves well (lower peak contact pressure values) under positive turnover moments and positive axial loads. Table 3 presents a comparison of the peak contact

pressure values of both joints (CJ₂ and BJ₆). In 37 % of the analysed cases (cells in light green colour in Table 3), CJ₂ had lower peak contact pressure with respect to the BJ₆, with a mean difference of 32 %. In 6 % of the cases (cells in light orange colour in Table 3), BJ₆ had lower peak contact pressure regarding the CJ₂, with a mean difference of 10 %. In 20 % of the cases (cells in dark orange colour in Table 3), BJ₆ did not converge while CJ₂ did. In 15 % of the cases (cells in dark green colour in Table 3) CJ₂ did not converge while BJ₆ did. Simulations did not converge for any of the joints in 22 % of the cases (blank cells in Table 3). Besides having a lower peak contact pressure, CJ₂ also had a wider load range (the simulations converged in more cases) and with a greater mean difference in pressure than BJ₆.

In Figure 12, the contact pressure distribution over the shafts of the CJ₂ and BJ₆ can be seen from the bottom view under their preferential loading conditions. The lowest contact pressure was obtained on the CJ₂, with a value of 55.65 MPa for loading conditions presented in the bottom part of the figure. These loading conditions correspond to a carrying angle of 30°. The contact under these conditions is characterized by two contact zones, with one larger than the other. The lowest value of BJ₆ was 76 MPa. The contact under these conditions is characterized by three contact zones, two large and one more narrow. These loading conditions correspond to a carrying angle of 15°.

4. Discussion and conclusions

In this study, the contact response of two groups of bio-inspired joints were analysed under application of external mechanical loads using FEM. The mechanical joints, inspired on the camel and bison elbow morphologies, behave differently during transmission of external loads.

The load bearing performance of the bison-inspired joints showed an asymmetrical response with respect to the zero axial load value. Similarly, an asymmetrical response of the same joints with respect to the zero turnover moment value was observed. This can be explained by the mid-sagittal plane asymmetry of the geometry of the joints. This shows a preferential loading side, which might be related with the physiological loading conditions of the studied joints. The obtained results from both joints showed that the carrying angle was not perpendicular to the rotation axis (around 15° for bison and 30° for camel) with medial-lateral loading inclination. Similar results were found for the human elbow, with an angle of 11-16° of medial-lateral loading (Ayhan and Ayhan, 2020).

The different morphological profiles extracted from the real bones showed that the morphology of the articular surface varies in function of the flexion-extension angle of the elbow. This variation translates into changes on the articular contact, which is in accordance with the results presented in (Goel et al., 1982).

It was found that the camel-inspired joint exhibited lower peak contact pressure values in a wider range than the bison-inspired joint. The camel-inspired joint presented larger contact areas than the bison-inspired joint, which might be caused by a greater congruence between the bearing and the shaft geometry (see Figure 6). The congruence of biological joints has been interpreted by MacConaill (1953) as a functional gap intentionally created to allow an efficient lubrication of the joint. This might suggest that the elbow of the bison is more suitable for high-speed operation than the camel elbow. Additionally, the maximal tangential speed on the bison-inspired joint surface is lower than that of the camel-inspired joint given that the maximum radii of this joint are smaller, and therefore less wear is produced (assuming equal material properties).

The bison-inspired joint showed to be more specialized for bearing positive turnover moments in absence of axial loads. This can be explained by the geometry at the right end of the joint, which presents a smaller curvature regarding the same zone of the camel-inspired joint (see capitellum in Figure 6-b).

Results showed that the camel-inspired joint is more suitable for supporting axial and combined loads. The capacity of the camel-inspired joint to bear axial loads can be explained by the groove derived from the capitellotrochlear sulcus that acts as a thrust collar. The depth of this groove is almost three times larger than that of the bison-inspired joint (see Δr_C and Δr_B in Figure 6). This generates a larger projection surface in the radial plane (a plane orthogonal to the rotation axis) and therefore a better capacity for bearing axial loads. Similar results were found by Willing et al. (2014), who tested a similar geometry to that of the camel elbow (hourglass) against other geometries (cylindrical and concave).

In technological applications of load bearing at high speeds (i.e., those requiring the use of roller bearings), certain arrangements of bearings present an equivalent contact topology to that of the camel and bison elbow. The topology of the camel-inspired profile can be associated with a back-to-back bearing arrangement (see Figure 13(a)), while the bison-inspired profile can be associated with a back-to-back and tandem bearing arrangement (see Figure 13(b)). In accordance with our results, the back-to-back arrangement allows axial force absorption in both directions and presents a good rigidity against turnover moments. On the other hand, back-to-back and tandem bearing arrangement present a reinforced capacity to absorb turnover moments. This kind of arrangements has not been tested yet in the case of sliding bearings (or bushing bearings) because of the associated difficulties in the manufacturing processes (machining and assembly). Nevertheless, technologies of nowadays allow to perform complex geometries by additive manufacturing or 5-axes CNC machining. So technological barriers have been knocked down opening the way for development of new designs.

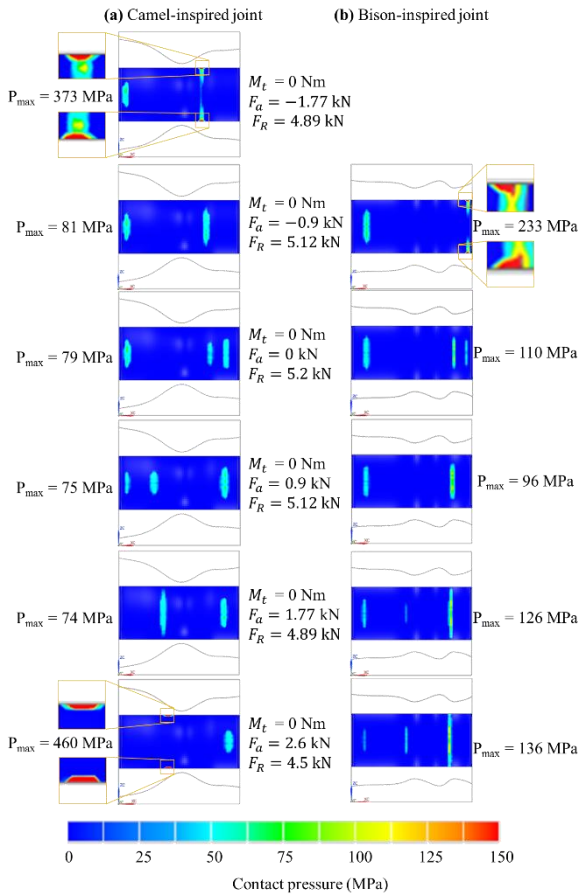


Figure 9: Pressure distribution under application of axial load for (a) camel-inspired joint and (b) bison-inspired joint. The applied load conditions (turnover moment, axial load and radial load) can be seen on the central section of the figure and were the same for camel and bison.

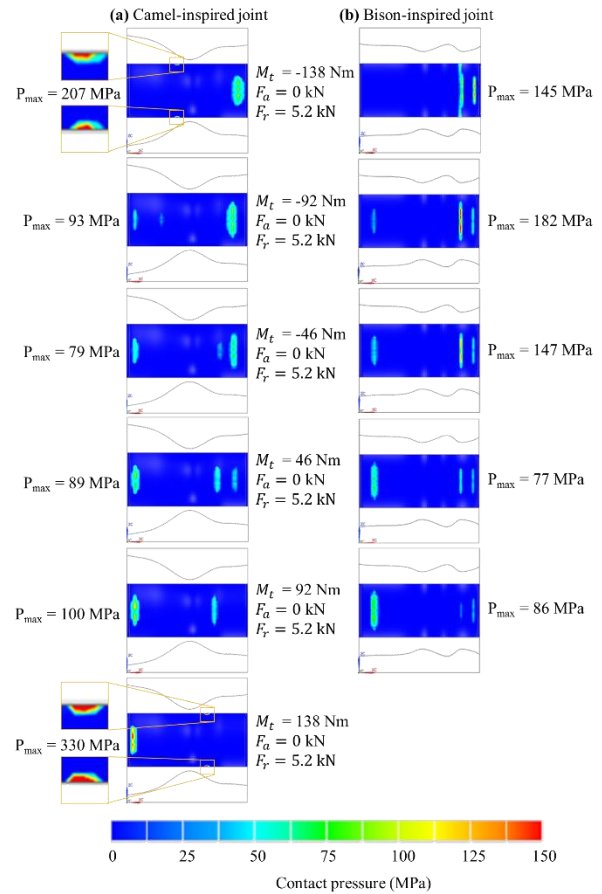


Figure 10: Pressure distribution under application of turnover moment for (a) camel-inspired joint and (b) bison-inspired joint. The applied load conditions (turnover moment, axial load and radial load) can be seen on the central section of the figure and were the same for camel and bison.

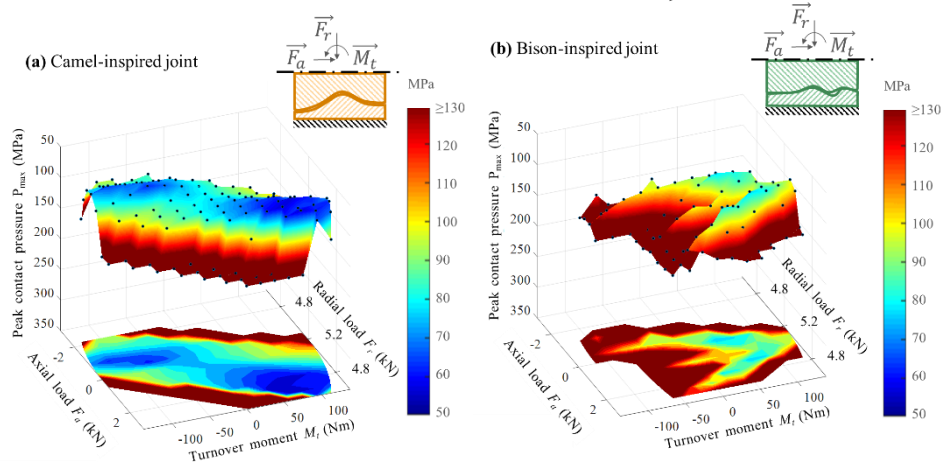


Figure 11: Peak contact pressure (in MPa) as a function of the applied axial load (in kN) (radial load as secondary axis (in kN)) and turnover moment (in Nm) for the camel-inspired joint (CJ₂ geometry) on the left-hand side and for the bison-inspired joint (BJ₆ geometry) on the right-hand side. The colour bar shows the peak contact pressure values from 50 MPa (in blue colour) to ≥ 130 MPa (in dark red colour). The axial load axis is represented on the horizontal axis on the left side of each graph. The range of the axial load goes from -3 kN to 3 kN. A secondary axis, parallel to the axial load axis represents the radial loads. The horizontal axis represents the turnover moment. Turnover moment range goes from -138 Nm to 138 Nm.

Table 3: Relative difference expressed in percentage of the peak contact pressure obtained with the camel-inspired and the bison-inspired joints. In light green colour: results when the bison-inspired joint had lower peak pressure. In light orange colour: results when the camel-inspired joint had lower peak pressure. In dark green colour and with the mark 'B': results when the simulation with the camel-inspired joint did not converge but the bison-inspired did. In dark orange colour and with the mark 'C': results when the simulation with the bison-inspired joint did not converge but the camel-inspired did. Empty white cells: none of the simulations converged.

	Fr (kN)	4.886	5.023	5.121	5.180	5.200	5.180	5.121	5.023	4.886	4.713	4.503
Fa (kN)	-1.779	-1.346	-0.903	-0.453	0.000	0.453	0.903	1.346	1.779	2.198	2.600	
M (Nm)												
Fr*(-26.5)	C	C	54.6	38.6	B	B						
Fr*(-22.1)	C	C	57.3	42.3	28.4	B	B					
Fr*(-17.7)	C	C	43.1	47.2	21.0	45.9	B	B	B			
Fr*(-13.3)	21.0	C	C	53.1	14.7	46.6	C	B	B	B	B	B
Fr*(-8.8)	30.3	C	C	49.1	20.2	42.9	57.4	8.1	B	B	B	B
Fr*(-4.4)	B	C	C	22.1	21.9	37.8	54.6	27.4	B	B	B	B
Fr*(0)		C	C	15.6	28.3	30.8	49.4	23.6	53.0	B	B	B
Fr*(4.4)			C	7.6	7.5	36.4	29.8	51.6	14.5	9.1		B
Fr*(8.8)			C	2.8	14.3	12.3	33.7	32.0	26.2	44.2	33.0	C
Fr*(13.3)				C	15.2	11.0	28.6	17.7	39.1	70.5		C
Fr*(17.7)					15.1	8.8	2.6	13.1	63.4	C	C	C
Fr*(22.1)					9.2	6.7	1.9	29.4	C	C	C	C
Fr*(26.5)						11.0	6.5	C	C	C	C	C

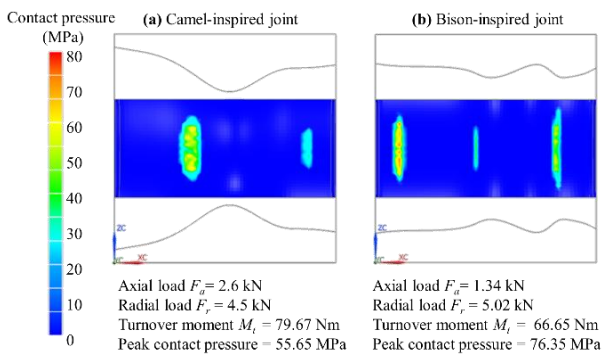


Figure 12: Contact pressure under the preferential loading conditions for the (a) CJ₂; (b) BJ₆. The colour bar represents the contact pressure value from 0 MPa (in blue colour) to 80 MPa (in red colour).

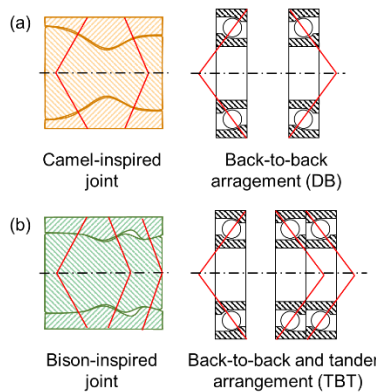


Figure 13: (a) Camel-inspired joints profile association with a back-to-back bearing arrangement; (b) Bison-inspired joints profile association with a back-to-back and tandem bearing arrangement. Red lines represent the contact angles.

In synovial joints, muscles and ligaments preserve their stability. In contrast, in technological cases, there are three feasible options to preserve the stability of revolute joints. The first option is to let a unilateral joint (the housing covers less than half of the shaft and hence can be separated from the housing), this option is feasible if the directions of the efforts are well known and they do not change during operation. This is case for example of some rotatory drum dryers. The second option is to build a bilateral joint which its housing (female part) is made of two half parts to allow the assembly process of the shaft (see for example Figure 2). The third option is to build a non-assembly joint by means of additive manufacturing. In this non-assembly joint, the male part is fabricated inside the female part with a controlled clearance. A manufacturability proof was done with the bison-inspired joint using additive manufacturing technology (Selective Laser Melting, SLM). The complete part was splinted at the end the process using electrical discharge machining for visualization purposes. The obtained joint is presented in Figure XX. This type of procedures is just being explored by the industrial and scientific community and needs more study (see, for example, Boschetto and Bottini (2019)).

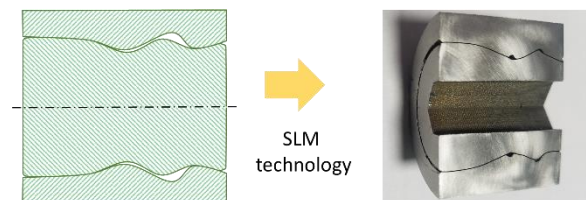


Figure 14. Manufacturability proof done with the bison-inspired joint using additive manufacturing technology (Selective Laser Melting, SLM).

This study presents several limitations. First, cartilage and soft tissues, which may influence load transmission performance, were not considered. However, as this is a comparative study, the cushioning effects generated by a softer material affect in equal manner both joints (assuming small deformations). Therefore, contact pressure values will change while the global tendency of the contact pressure regarding the external loads will not. This can be assumed if the topology of the contact (number of contact zones) does not change. This is the case when the deformations are small regarding the curvature of the contacting profile and it corresponds to the assumption of the present work. Therefore, in the case of very soft materials or very high loads, the topology of the contact (the number of contact zones) may change, and the load bearing response of the joint will be different. The former case was not addressed in this work, but it merits further investigation. Therefore, future work is required to determine the role of cartilage in pressure distribution, which might help to improve the designs of bio-inspired mechanical joints. The study of the contact mechanics of articular cartilage can be done in vitro, for example, using x-ray reconstruction of moving morphology as demonstrated by Tsai et al. (2020).

A second limitation is that the application of the applied external load was assumed to belong to the same plane. In most industrial application the radial load and turnover moment act in the same plane, which is in accordance with this assumption. For future studies, the load bearing behaviour of the joints must be explored while loads are applied from different planes. Future work is also required to develop a methodology for the design of bio-inspired mechanical joints that allows to synthesize geometrical parameters (congruency, geometrical symmetry, profile curvatures, depth of grooves) of kinematical joints in function of the loading conditions.

In conclusion, kinematically equivalent biological joints can present different morphologies that make each one the optimal compromise for the loading conditions. Learning about the natural rules of mechanical design can provide new insights to improve the design of current mechanical joints.

Competing interests

The authors have declared that no competing interests exist.

References

- Adouni, M., Shirazi-Adl, A., Shirazi, R., 2012. Computational biodynamics of human knee joint in gait: From muscle forces to cartilage stresses. *Journal of Biomechanics* 45, 2149–2156. <https://doi.org/10.1016/j.jbiomech.2012.05.040>
- Alcid, J.G., Ahmad, C.S., Lee, T.Q., 2004. Elbow anatomy and structural biomechanics. *Clinics in Sports Medicine* 23, 503–517. <https://doi.org/10.1016/j.csm.2004.06.008>
- Amirudin, A.N., Parasuraman, S., Kadirvel, A., Khan, M.K.A.A., Elamvazuthi, I., 2014. Biomechanics of Hip, Knee and Ankle Joint Loading during Ascent and Descent Walking. *Procedia Computer Science* 42, 336–344. <https://doi.org/10.1016/j.procs.2014.11.071>
- Andersson, K., 2004. Elbow-joint morphology as a guide to forearm function and foraging behaviour in mammalian carnivores. *Zoological Journal of the Linnean Society* 142, 91–104. <https://doi.org/10.1111/j.1096-3642.2004.00129.x>
- Au, S., Berniker, M., Herr, H., 2008. Powered ankle-foot prosthesis to assist level-ground and stair-descent gaits. *Neural Networks* 21, 654–666. <https://doi.org/10.1016/j.neunet.2008.03.006>
- Ayhan, E., Ayhan, Ç., 2020. Kinesiology of the elbow complex, in: *Comparative Kinesiology of the Human Body*. Elsevier, pp. 191–210. <https://doi.org/10.1016/B978-0-12-812162-7.00012-6>
- Becker, J., Mermoz, E., Linares, J.-M., 2019. Joint Loading Estimation Method for Horse Forelimb High Jerk Locomotion: Jumping. *Journal of Bionic Engineering* 16, 1143–1143. <https://doi.org/10.1007/s42235-019-0125-1>
- Boedo, S., Eshkabilov, S.L., 2003. Optimal Shape Design of Steadily Loaded Journal Bearings using Genetic Algorithms. *Tribology Transactions* 46, 134–143. <https://doi.org/10.1080/10402000308982610>
- Boschetto, A., Bottini, L., 2019. Manufacturability of non-assembly joints fabricated in AlSi10Mg by selective laser melting. *Journal of Manufacturing Processes* 37, 425–437. <https://doi.org/10.1016/j.jmappro.2018.12.021>
- Bruyas, A., Geiskopf, F., Renaud, P., 2015. Design and Modeling of a Large Amplitude Compliant Revolute Joint: The Helical Shape Compliant Joint. *Journal of Mechanical Design* 137. <https://doi.org/10.1115/1.4030650>
- Cil, A., Veillette, C.J., Sanchez-Sotelo, J., Morrey, B.F., 2008. Linked Elbow Replacement: A Salvage Procedure for Distal Humeral Nonunion: The Journal of Bone and Joint Surgery-American Volume 90, 1939–1950. <https://doi.org/10.2106/JBJS.G.00690>
- Dragoni, E., 2013. Optimal design of radial cylindrical roller bearings for maximum load-carrying capacity. *Proceedings of the Institution of Mechanical Engineers, Part C: Journal of Mechanical Engineering Science* 227, 2393–2401. <https://doi.org/10.1177/0954406213477579>
- Egan, P., Sinko, R., LeDuc, P.R., Keten, S., 2015. The role of mechanics in biological and bio-inspired systems. *Nature Communications* 6. <https://doi.org/10.1038/ncomms8418>
- Fesanghary, M., Khonsari, M.M., 2013. On the optimum groove shapes for load-carrying capacity enhancement in parallel flat surface bearings: Theory and experiment. *Tribology International* 67, 254–262. <https://doi.org/10.1016/j.triboint.2013.08.001>
- Fujiwara, S., 2009. Olecranon orientation as an indicator of elbow joint angle in the stance phase, and estimation of forelimb posture in extinct quadruped animals. *Journal of Morphology* 270, 1107–1121. <https://doi.org/10.1002/jmor.10748>
- Gherca, A., Fatu, A., Hajjam, M., Maspeyrot, P., 2013. Influence of Surface Geometry on the Hydrodynamic Performances of Parallel Bearings in Transient Flow Conditions. *Tribology Transactions* 56, 953–967. <https://doi.org/10.1080/10402004.2013.813997>

- Goel, V.K., Singh, D., Bijlani, V., 1982. Contact Areas in Human Elbow Joints. *Journal of Biomechanical Engineering* 104, 169–175. <https://doi.org/10.1115/1.3138344>
- Granatosky, M.C., McElroy, E.J., Laird, M.F., Iriarte-Diaz, J., Reilly, S.M., Taylor, A.B., Ross, C.F., 2019. Joint angular excursions during cyclical behaviors differ between tetrapod feeding and locomotor systems. *J Exp Biol* 222. <https://doi.org/10.1242/jeb.200451>
- Harrison, S.M., Whitton, R.C., Kawcak, C.E., Stover, S.M., Pandey, M.G., 2010. Relationship between muscle forces, joint loading and utilization of elastic strain energy in equine locomotion. *Journal of Experimental Biology* 213, 3998–4009. <https://doi.org/10.1242/jeb.044545>
- Haut Donahue, T.L., Hull, M.L., Rashid, M.M., Jacobs, C.R., 2002. A Finite Element Model of the Human Knee Joint for the Study of Tibio-Femoral Contact. *Journal of Biomechanical Engineering* 124, 273–280. <https://doi.org/10.1115/1.1470171>
- Hili, M.A., Fakhfakh, T., Hammami, L., Haddar, M., 2005. Shaft misalignment effect on bearings dynamical behavior. *The International Journal of Advanced Manufacturing Technology* 26, 615–622. <https://doi.org/10.1007/s00170-004-2013-y>
- Lerner, Z.F., Gadowski, B.C., Ipson, A.K., Haussler, K.K., Puttlitz, C.M., Browning, R.C., 2015. Modulating tibiofemoral contact force in the sheep hind limb via treadmill walking: Predictions from an opensim musculoskeletal model. *Journal of Orthopaedic Research* 33, 1128–1133. <https://doi.org/10.1002/jor.22829>
- Lin, J.-R., 2001. Optimal design of one-dimensional porous slider bearings using the Brinkman model. *Tribology International* 34, 57–64. [https://doi.org/10.1016/S0301-679X\(00\)00138-9](https://doi.org/10.1016/S0301-679X(00)00138-9)
- Maas, S.A., Ellis, B.J., Rawlins, D.S., Weiss, J.A., 2016. Finite element simulation of articular contact mechanics with quadratic tetrahedral elements. *Journal of Biomechanics* 49, 659–667. <https://doi.org/10.1016/j.jbiomech.2016.01.024>
- MacConaill, M.A., 1953. The movements of bones and joints: 5. The Significance of Shape. *The Journal of Bone and Joint Surgery*. British volume 35-B, 290–297. <https://doi.org/10.1302/0301-620X.35B2.290>
- Mason, D.R., Schulz, K.S., Fujita, Y., Kass, P.H., Stover, S.M., 2005. In vitro force mapping of normal canine humeroradial and humeroulnar joints. *American Journal of Veterinary Research* 66, 132–135. <https://doi.org/10.2460/ajvr.2005.66.132>
- Masouros, S.D., Bull, A.M.J., Amis, A.A., 2010. (i) Biomechanics of the knee joint. *Orthopaedics and Trauma* 24, 84–91. <https://doi.org/10.1016/j.mporth.2010.03.005>
- Mermoz, E., Fages, D., Zamponi, L., Linares, J.-M., Sprauel, J.-M., 2016. New methodology to define roller geometry on power bearings. *CIRP Annals* 65, 157–160. <https://doi.org/10.1016/j.cirp.2016.04.095>
- Mesfar, W., Shirazi-Adl, A., 2005. Biomechanics of the knee joint in flexion under various quadriceps forces. *The Knee* 12, 424–434. <https://doi.org/10.1016/j.knee.2005.03.004>
- Messaoud, N.B., Bouaziz, S., Fakhfakh, T., Maatar, M., Haddar, M., 2011. Dynamic behavior of active magnetic bearings in presence of angular misalignment defect. *International Journal of Applied Mechanics* 03, 491–505. <https://doi.org/10.1142/S1758825111001093>
- Nia, H.T., Han, L., Li, Y., Ortiz, C., Grodzinsky, A., 2011. Poroelasticity of Cartilage at the Nanoscale. *Biophysical Journal* 101, 2304–2313. <https://doi.org/10.1016/j.bpj.2011.09.011>
- Panagiotopoulou, O., Rankin, J.W., Gatesy, S.M., Hutchinson, J.R., 2016. A preliminary case study of the effect of shoe-wearing on the biomechanics of a horse's foot. *PeerJ* 4, e2164. <https://doi.org/10.7717/peerj.2164>
- Papadopoulos, C.I., Efstathiou, E.E., Nikolakopoulos, P.G., Kaiktsis, L., 2011. Geometry Optimization of Textured Three-Dimensional Micro-Thrust Bearings. *Journal of Tribology* 133. <https://doi.org/10.1115/1.4004990>
- Patel, B.A., 2005. The hominoid proximal radius: re-interpreting locomotor behaviors in early hominins. *Journal of Human Evolution* 48, 415–432. <https://doi.org/10.1016/j.jhevol.2005.01.001>
- Picault, E., Mermoz, E., Thouveny, T., Linares, J.-M., 2018. Smart pressure distribution estimation in biological joints for mechanical bio-inspired design. *CIRP Annals* 67, 153–156. <https://doi.org/10.1016/j.cirp.2018.04.116>
- Poncercy, B., Arroyave-Tobón, S., Picault, E., Linares, J.-M., 2019. Effects of realistic sheep elbow kinematics in inverse dynamic simulation. *PLOS ONE* 14, e0213100. <https://doi.org/10.1371/journal.pone.0213100>
- Poplawski, J.V., Peters, S.M., Zaretsky, E.V., 2001. Effect Of Roller Profile On Cylindrical Roller Bearing Life Prediction—Part I: Comparison of Bearing Life Theories. *Tribology Transactions* 44, 339–350. <https://doi.org/10.1080/10402000108982466>
- Potočník, R., Göncz, P., Flašker, J., Glodež, S., 2010. Fatigue life of double row slewing ball bearing with irregular geometry. *Procedia Engineering* 2, 1877–1886. <https://doi.org/10.1016/j.proeng.2010.03.202>
- Praet, T., Adriaens, D., Cauter, S.V., Masschaele, B., Beule, M.D., Verheghe, B., 2012. Inspiration from nature: dynamic modelling of the musculoskeletal structure of the seahorse tail. *International Journal for Numerical Methods in Biomedical Engineering* 28, 1028–1042. <https://doi.org/10.1002/cnm.2499>
- Prasad, N., Ali, A., Stanley, D., 2016. Total elbow arthroplasty for non-rheumatoid patients with a fracture of the distal humerus: a minimum ten-year follow-up. *The Bone & Joint Journal* 98-B, 381–386. <https://doi.org/10.1302/0301-620X.98B3.35508>
- Qiu, M., Raeymaekers, B., 2015. The load-carrying capacity and friction coefficient of incompressible textured parallel slider bearings with surface roughness inside the texture features. *Proceedings of the Institution of Mechanical Engineers, Part J: Journal of Engineering Tribology* 229, 547–556. <https://doi.org/10.1177/1350650114545352>
- Rezaei, A., Van Paepegem, W., De Baets, P., Ost, W., Degrieck, J., 2012. Adaptive finite element simulation of wear evolution in radial sliding bearings. *Wear* 296, 660–671. <https://doi.org/10.1016/j.wear.2012.08.013>
- Russell, F., Zhu, Y., Hey, W., Vaidyanathan, R., Ellison, P., 2018. A biomimicking design for mechanical knee joints. *Bioinspiration & Biomimetics* 13, 056012. <https://doi.org/10.1088/1748-3190/aad39d>
- Sancho-Bru, J.L., Pérez-González, A., Vergara-Monedero, M., Giurintano, D., 2001. A 3-D dynamic model of human finger for studying free movements. *Journal of Biomechanics* 34, 1491–1500. [https://doi.org/10.1016/S0021-9290\(01\)00106-3](https://doi.org/10.1016/S0021-9290(01)00106-3)
- Sathasivam, S., Walker, P.S., 1994. Optimization of the bearing surface geometry of total knees. *Journal of Biomechanics*

- 27, 255–264. [https://doi.org/10.1016/0021-9290\(94\)90002-7](https://doi.org/10.1016/0021-9290(94)90002-7)
- Tsai, H.P., Turner, M.L., Manafzadeh, A.R., Gatesy, S.M., 2020. Contrast-enhanced XROMM reveals *in vivo* soft tissue interactions in the hip of *Alligator mississippiensis*. *J. Anat.* 236, 288–304. <https://doi.org/10.1111/joa.13101>
- Wang, X., Kato, K., Adachi, K., Aizawa, K., 2003. Loads carrying capacity map for the surface texture design of SiC thrust bearing sliding in water. *Tribology International* 36, 189–197. [https://doi.org/10.1016/S0301-679X\(02\)00145-7](https://doi.org/10.1016/S0301-679X(02)00145-7)
- Wei, X., Tian, Y., Joneja, A., 2016. A study on revolute joints in 3D-printed non-assembly mechanisms. *Rapid Prototyping Journal* 22, 901–933. <https://doi.org/10.1108/RPJ-10-2014-0146>
- Willing, R., King, G.J.W., Johnson, J.A., 2014. The effect of implant design of linked total elbow arthroplasty on stability and stress: a finite element analysis. *Computer Methods in Biomechanics and Biomedical Engineering* 17, 1165–1172. <https://doi.org/10.1080/10255842.2012.739161>
- Zamponi, L., Mermoz, E., Linares, J.M., Sprauel, J.M., 2009. Impact of geometrical defects on bearing assemblies with integrated raceways in aeronautical gearboxes. *Mechanism and Machine Theory* 44, 1108–1120. <https://doi.org/10.1016/j.mechmachtheory.2008.10.005>
- Zupan, S., Prebil, I., 2001. Carrying angle and carrying capacity of a large single row ball bearing as a function of geometry parameters of the rolling contact and the supporting structure stiffness. *Mechanism and Machine Theory* 36, 1087–1103. [https://doi.org/10.1016/S0094-114X\(01\)00044-1](https://doi.org/10.1016/S0094-114X(01)00044-1)

Appendix A

Reference to the collection of National Museum of Natural History in Paris.

Species	Reference to the collection of National Museum of Natural History in Paris
<i>Antilope cervicapra</i>	MNHN-ZM-AC-1888-734
<i>Bison bison</i>	MNHN-ZM-AC-1951-242
<i>Connochoates gnou</i>	MNHN-ZM-AC-1976-344
<i>Diceros bicornis</i>	MNHN-ZM-AC-1944-278
<i>Equus caballus</i>	MNHN-ZM-AC-1932-46
<i>Rhinoceros unicornis</i>	MNHN-ZM-AC-1885-734
<i>Camelus bactrianus</i>	MNHN-ZM-AE-2007-1435
<i>Elephas maximus</i>	MNHN-ZM-1896-17